14th International Symposium on Turbulence and Shear Flow Phenomena (TSFP14)
Heidelberg, Germany, July 28–31, 2026

DYNAMIC STALL ONSET DELAY IN TURBULENT ENVIRONMENTS

Sahar Rezapour
Mechanical Engineering
EPFL
Lausanne, Switzerland
sahar.rezapour@epfl.ch

Karen Mulleners
Mechanical Engineering
EPFL
Lausanne, Switzerland
karen.mulleners@epfl.ch

ABSTRACT

Dynamic stall is the delayed flow separation that occurs on airfoils undergoing rapid changes in angle of attack. The delay between the instant the critical stall angle is exceeded and the onset of dynamic stall scales with the non-dimensional pitch rate as a power law. This delay scaling has been characterised under low-turbulence inflow conditions. We extend this characterisation to turbulent inflow conditions through force measurements on a pitching NACA 0018 airfoil under three grid-generated turbulent inflows. The critical stall angle measured with quasi-static angle of attack variations shifts to higher angles of attack when the turbulence intensity in increased in the free-stream, from 14° in the low-turbulent inflow without grid to 20° in the turbulent inflow generated by the coarsest grid. The stall onset delay follows a common power-law scaling with pitch rate when calculated with respect to the quasi-steady stall angle threshold measured for the specific inflow conditions. Free-stream turbulence shifts the critical threshold for static stall initiation but preserves the power-law scaling of the dynamic stall onset as a function of the pitch rate under unsteady conditions.

1 Introduction

Aerodynamic surfaces operating in realistic environments are exposed to inflow disturbances. Wind turbines operate within atmospheric boundary layers containing turbulent velocity fluctuations generated by upstream turbines, terrain, and built structures (Porté-Agel *et al.*, 2020; Nedic *et al.*, 2024; Revaz & Porté-Agel, 2024). The wakes of upstream turbines introduce velocity deficits, coherent vortices, and turbulence, which alter the effective inflow experienced by downstream blades. For horizontal-axis wind turbines, this turbulent environment has been studied mainly through its effect on wake recovery and power output (Vahidi & Porté-Agel, 2024; Shamsoddin & Porté-Agel, 2018; Dar *et al.*, 2025). For vertical-axis wind turbines, turbulence also influences the separation process on the individual blades.

Free-stream turbulence affects the formation, transition, and separation of the boundary layer and influences the aerodynamic behaviour of wings and blades (Yu *et al.*, 2017; Istvan & Yarusevych, 2018; Huang *et al.*, 2020). Turbulence promotes boundary-layer transition, and makes the boundary layer more resistant to adverse pressure gradients (Kay *et al.*, 2020; Toppings & Yarusevych, 2025). The transition location depends not only on turbulence intensity but also on the integral length scale, which can either advance or delay transition depending on its ratio to the boundary-layer thickness (Fransson & Shahinfar, 2020). The enhanced boundary layer resistance shifts stall onset to higher angles of attack and increases the maximum lift coefficient (Devinant *et al.*, 2002; Thompson *et al.*, 2023). Wind tunnel measurements on a wind turbine blade section at chord-based Reynolds numbers between 1.3×10^5 and 3×10^5 confirm that increasing turbulence intensity from 0.3 % to 3 % delays the stall angle and smoothens the lift curve near stall (Mishra *et al.*, 2022). For a NACA 0018 airfoil at a transitional Reynolds number, elevated turbulence suppresses static hysteresis and shifts both stall and reattachment to higher angles of attack (Damiola *et al.*, 2023).

Vertical axis wind turbines operating at low tip-speed ratios experience dynamic stall during each cycle of rotation (Le Fouest & Mulleners, 2022). Dynamic stall involves delayed leading-edge separation, the formation of a leading-edge vortex, and a rapid reduction in lift when the vortex is convected downstream. Increased turbulence intensity shifts the formation of the leading-edge vortex to higher angles of attack (Yu *et al.*, 2017; Huang *et al.*, 2020). Direct numerical simulations of a pitching airfoil in the wake of an upstream cylinder show that wake turbulence delays dynamic stall onset and produces a weaker dynamic stall vortex compared to undisturbed inflow (Gandhi *et al.*, 2017). At the turbine scale, the delayed stall onset increases aerodynamic performance (Ahmadi-Baloutaki *et al.*, 2015; Nedic *et al.*, 2024). Turbulent inflow produces smaller and less coherent leading-edge vortices and increases turbulent kinetic energy near the airfoil surface, which promotes earlier reattachment when the angle of attack is decreased (Yu *et al.*, 2017; Huang *et al.*, 2020; Damiola *et al.*, 2023). The earlier reattachment is attributed to enhanced mixing and entrainment in the separated shear layer, which increases momentum transport towards the surface (Vita *et al.*, 2020). These changes modify the magnitude and timing of unsteady aerodynamic loads.

Dynamic stall onset delay is measured relative to the quasi-steady stall threshold, and the delay is governed by the pitch rate. This delay follows a power-law scaling with the non-dimensional pitch rate (Le Fouest *et al.*, 2021; Ayancik & Mulleners, 2022; Rezapour & Mulleners, 2025). This power-law scaling of the stall onset delay with pitch rate has previously only been determined in clean inflow conditions. The influence of free-stream turbulence on this scaling remains to be determined.

Here, we examine how free-stream turbulence modifies static stall thresholds and the dynamic stall onset delay. Grid-generated turbulence is used to produce controlled inflow conditions with varying turbulence intensities and integral length scales. Quasi-static measurements are performed to quantify shifts in stall and reattachment angles under turbulent inflows. Measurements of dynamically pitching airfoils are performed to examine how stall onset delay scales with the non-dimensional pitch rate for various inflow conditions.

2 Methods

Experiments were conducted in the SHARX recirculating water channel at EPFL, which has a $0.6\,\mathrm{m} \times 0.6\,\mathrm{m} \times 3\,\mathrm{m}$ test section. A NACA0018 airfoil with chord length $c = 0.15\,\mathrm{m}$ and span $s = 0.58\,\mathrm{m}$ was mounted vertically in the test section. The blade tip was positioned close to the bottom of the channel to limit tip vortices. A splitter plate was installed at the blade root to eliminate surface effects. The flow velocity was $\mathrm{U}_\infty = 0.4\,\mathrm{m/s}$, corresponding to a chord-based Reynolds number of $Re = 60\,000$. At this Reynolds number, laminar separation bubbles can form. Zigzag tripping tape with a thickness of 0.8 mm was applied on both the suction and the pressure side near the maximum thickness location to enforce boundary layer transition and eliminate the laminar separation bubble. Aerodynamic forces were measured using a six-component ATI Nano 25 load cell with a sampling frequency of 1000 Hz, a sensing range of 125 N, and a resolution of 0.02 N.

Quasi-static measurements were conducted to obtain static lift polars and to determine the critical static stall and static reattachment angles. The angle of attack of the airfoil was changed in discrete steps of 0.5°, from $\alpha = 0°$ to 30° during pitch-up and from 30° to 0° during pitch-down. At each step, aerodynamic forces were recorded for 20 s. This duration corresponds to ≈ 53 convective times ($\frac{\mathrm{U}_\infty}{c}$). The mean lift coefficient and its standard deviation were computed from these measurements. Dynamic pitching tests were performed by pitching the airfoil about its quarter-chord axis using linear ramp motions from $\alpha = 0°$ to $\alpha_{\max} = 30°$. The non-dimensional pitch rates of the tested ramp motions, defined as $(\dot{\alpha}c)/(2\mathrm{U}_\infty)$, was varied between 0.0008 and 0.01. The measurements were repeated five times per pitch rate to assess uncertainty.

Free-stream turbulence was generated using three regular square-mesh grids placed 800 mm upstream of the airfoil leading-edge. The grids had mesh sizes $M = 45\,\mathrm{mm}$, 90 mm, and 180 mm with a solidity of 30 %, corresponding to $M/c = 0.3$, 0.6, and 1.2. The normalised downstream distance from the grid to the airfoil location was $x/M = 17.8$, 8.9, 4.4 for the fine, medium, and coarse grids, respectively. The ratio x/M characterises the stage of turbulence development downstream of the grid. The wake structures generated by the grid interact and merge as x/M increases, leading to more homogeneous turbulence. The turbulence intensity decreases and the integral length scale increases with increasing x/M due to the decay and spatial evolution of turbulent kinetic energy (Mohamed & Larue, 1990). The present values of x/M indicate that the turbulence at the airfoil location is within the developing and early decay region of grid-generated turbulence. The coarse grid ($x/M = 4.4$) produces turbulence dominated by larger energetic structures, and the fine grid ($x/M = 17.8$) produces more evolved turbulence with smaller relative structure size and lower energy levels.

The turbulence characteristics of these grids were previously quantified in the same facility using particle image velocimetry (PIV). The streamwise turbulence intensity is defined as $Tu = u_{\mathrm{rms}}/\mathrm{U}_\infty$, where u_{rms} is the root-mean-square of the streamwise velocity fluctuations. The streamwise integral length scale $L_{11,1}$ represents the characteristic size of the dominant turbulent structures. The measurements to determine the turbulence intensity and the integral length scales were performed 1115 mm downstream of the grids Nedic *et al.* (2024). The streamwise integral length scales ($L_{11,1}$) were measured to be 38 mm, 40 mm, and 57 mm for the three grids, and the corresponding turbulence intensities were 3.2 %, 6.5 %, and 12.3 %. The baseline turbulence intensity in the channel without a grid was approximately 1 %.

The present measurements were conducted at a closer downstream location ($x = 800\,\mathrm{mm}$), where grid-generated turbulence is expected to have higher turbulence intensity and slightly smaller integral length scales due to the downstream decay of turbulent kinetic energy and the spatial evolution of the flow (Mohamed & Larue, 1990). The turbulence intensities at the airfoil location are expected to be slightly higher than the previously reported values, but preserving the relative differences between grid configurations. The coarse grid produces the largest turbulence structures and the highest turbulence intensity, and the fine grid produces smaller-scale, lower-intensity turbulence.

Throughout this paper, the term baseline inflow condition refers to the flow in the absence of a turbulence-generating grid. Turbulent inflow conditions refer to the flows generated downstream of the turbulence grids.

3 Results

3.1 Static stall behaviour

The influence of the free-stream turbulence is first studied for the static lift polars obtained during quasi-static pitch-up and pitch-down motions for four inflow conditions. These inflow conditions include the baseline inflow (no grid) and three turbulent inflow conditions generated by grids with mesh sizes $M = 45\,\mathrm{mm}$, 90 mm, and 180 mm (fig. 1). Mean values are shown with markers, and shaded bands represent the standard deviation of the lift coefficient at each angle of attack, computed from measurements taken during 20 s at each step.

The lift coefficient increases linearly with angle of attack for the pitch-up polars for all inflow conditions up to $\approx 10°$ (fig. 1a). The mean lift coefficients collapse onto a single curve in the pre-stall region. The slope of this region is 1.9π determined based on the linear part of the lift. Free-stream turbulence does not modify the lift response when the flow is attached. The standard deviation bands reflect the degree of lift fluctuations. The lift measured under the baseline inflow condition shows the narrowest uncertainty band, and the lift measured under the inflow generated by the coarse grid ($M = 180\,\mathrm{mm}$) shows the widest band throughout the pre-stall and post-stall regions. As the angle of attack increases further, the lift curves reach a maximum and transition into stall.

The transition from attached flow to separated flow decreases the C_{L} during quasi-static pitch-up. We define the crit-

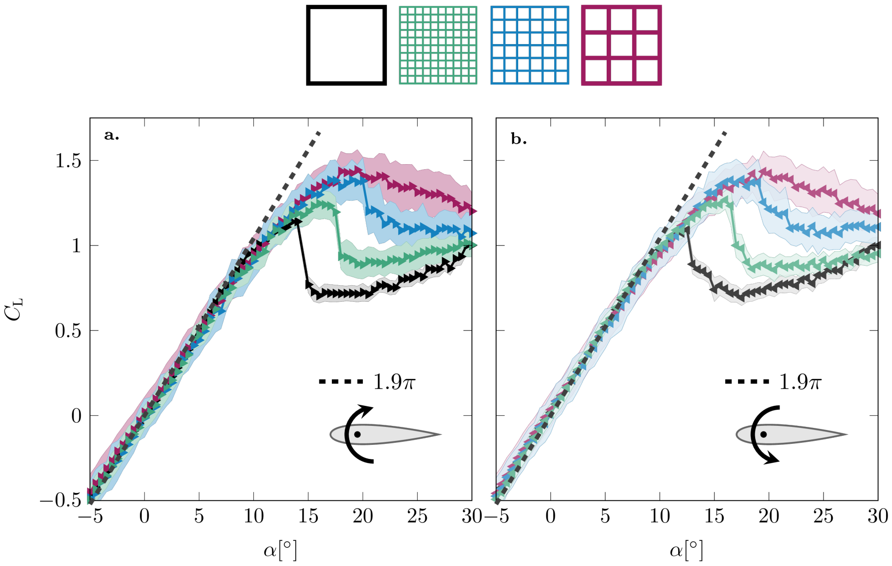

Figure 1. Static lift coefficient (C_L) polars for varying inflow conditions. The data are split into (a) polars obtained for the airfoil pitching up from 0° to 30° and (b) poloars obtained for the airfoil pitching down from 30° to 0°. Shaded bands indicate the standard deviation of the lift fluctuations. The visual legend at the top indicated the passive turbulence grids, ranging from the baseline (no grid) inflow condition to the turbulent flow generated with the coarse-mesh.

ical stall angle as the angle of attack at which the decrease begins. The lift curves obtained under the baseline inflow condition and under the inflow generated by the fine and medium grids ($M = 45$ mm and 90 mm) experience an abrupt drop in C_L, which provides a clear stall angle. The lift curve obtained under the inflow generated by the coarse grid ($M = 180$ mm) shows a smooth transition rather than a distinct drop. The airfoil operating under the baseline inflow condition stalls at $\alpha = 14°$. In the inflow generated by the fine grid ($M = 45$ mm), the stall is delayed to $\alpha = 17.5°$, and in the flow generated by the medium grid $M = 90$ mm the stall is further delayed to $\alpha = 20°$. Under the inflow generated by the coarse grid ($M = 180$ mm), the lift curve transitions smoothly from increasing to decreasing at $\alpha \approx 20°$ without an abrupt loss of lift. After crossing the critical stall angles, the flow is considered separated. In this separated-flow region, the mean lift coefficient remains higher under turbulent inflow conditions than under the baseline inflow condition. At a given angle of attack, the mean lift coefficient increases with mesh size, indicating that stronger turbulence enhances momentum exchange within the separated shear layer. As the angle of attack approaches $\alpha = 30°$, the lift coefficients converge for all inflow conditions.

The separated flow reattaches when the angle of attack is decreased (fig. 1b). For the pitch down polar, α is decreased from 30°, where the flow is fully separated. Reattachment occurs at a critical angle, where the separated shear layer reattaches to the airfoil surface (Rezapour & Mulleners, 2026). This transition produces an abrupt increase in C_L, which we use to identify the critical reattachment angle (fig. 1b). Reattachment occurs at $\alpha = 13°$ under the baseline inflow condition. Under the inflow generated by the fine, medium, and coarse grids, the reattachment occurs at $\alpha = 17°$, $\alpha = 19.5°$, and $\alpha = 21°$, respectively. The critical reattachment angles follow a similar trend as the critical stall angles variation, shifting toward higher angles of attack for increasing turbulence intensity and integral length scale. This shift indicates that turbulent inflow modifies both separation and reattachment, which changes the angular lag between these two events. The difference between the stall and reattachment angles is called the static hysteresis.

3.2 Stall onset in dynamic pitching

The effect of free-stream turbulence on the dynamic lift response is examined for two example non-dimensional pitch rates, $(\dot{\alpha}c)/(2U_\infty) = 0.003$ and $(\dot{\alpha}c)/(2U_\infty) = 0.009$. The ensemble-averaged evolutions of the lift coefficient for the baseline inflow condition and the three turbulent inflow conditions are shown in fig. 2. The coloured shaded bands around each mean curve indicate the uncertainty range, defined as the minimum and maximum lift coefficients recorded across the five repetitions. The vertical grey band marks the estimated stall onset transition window, determined from the power-law scaling for each pitch rate case (eq. (1)).

In the attached-flow regime, the lift coefficient increases again linearly with angle of attack for all inflow conditions (fig. 2a,c). The pre-stall lift curves collapse onto a single curve across all configurations, consistent with the static observations. Free-stream turbulence does not modify the attached-flow lift response under dynamic pitching. The responses under different inflow conditions diverge at higher angles of attack, where the inflow turbulence delays the separation onset. The dynamic stall angles shift toward higher values with increasing mesh size, following the same trend observed in the static results. The baseline inflow condition stalls first, followed sequentially by the fine, medium, and coarse grid configurations.

The lift reaches a maximum before decreasing when separation develops. At $(\dot{\alpha}c)/(2U_\infty) = 0.003$, a distinct lift drop is observed under the baseline and fine grid inflow conditions, whereas the coarse grid condition produces a more gradual decrease, resulting in a smoother transition from attached to separated flow similar to what was observed for the static behaviour (fig. 2a). At $(\dot{\alpha}c)/(2U_\infty) = 0.009$, the lift drops sharply at dynamic stall under all inflow conditions, including the coarse grid configuration (fig. 2c). This abrupt drop indicates that leading-edge vortex formation and shedding gov-

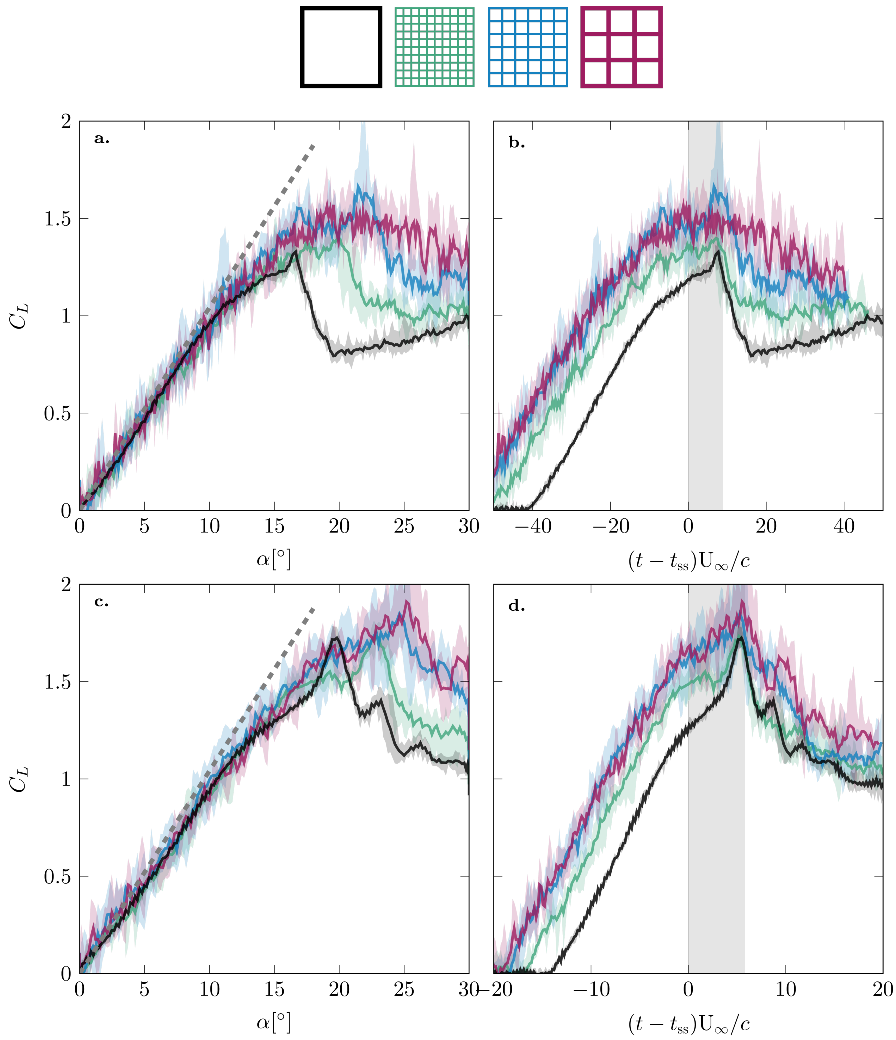

Figure 2. Effect of free-stream turbulence on the ensemble-averaged lift coefficient during the pitch-up phase for non-dimensional pitch rates of $(\dot{\alpha}c)/(2U_\infty) = 0.003$ (a,b) and $(\dot{\alpha}c)/(2U_\infty) = 0.009$ (c,d). The lift coefficient averaged over five repetitions is plotted against angle of attack α [°] (a,c), and convective time shifted by the instant the critical stall angle is exceeded $(t-t_{ss})U_\infty/c$ (b,d). The vertical grey band marks the estimated stall onset transition window from the power-law scaling for each pitch rate case. The dashed lines in (a) and (c) show the attached-flow lift slope 1.9π determined from the static polar under baseline inflow conditions.

ern stall onset at higher pitch rates, and turbulence does not suppress this vortex-driven mechanism. The lift fluctuations in the separated-flow region at $(\dot{\alpha}c)/(2U_\infty) = 0.009$ indicate the subsequent leading-edge vortex formation and detachment following the initial dynamic stall vortex detachment (Henne *et al.*, 2018).

To examine how turbulence modifies the temporal dynamics of stall onset, the lift coefficients are plotted against convective time shifted by the instant the configuration-specific static stall angle is exceeded, t_{ss}. When we plot the lift responses versus $(t-t_{ss})U_\infty/c$, the first lift peaks align across all inflow conditions (fig. 2b,d). This alignment indicates that once the quasi-steady stall threshold of each inflow condition is exceeded, dynamic stall develops after a comparable convective time delay, independent of turbulence level.

We now characterise the stall onset angle, maximum lift coefficient, and stall delay across all tested pitch rates. These parameters are presented as a function of the non-dimensional pitch rate $(\dot{\alpha}c)/(2U_\infty)$ in fig. 3. The mean values over five repetitions per pitch rate case are indicated with markers, and the error bars indicate the standard deviations across repetitions.

The dynamic stall angles α_{ds} increase with increasing $(\dot{\alpha}c)/(2U_\infty)$ for all configurations (fig. 3a), which is consistent with the classical pitch-rate dependence of dynamic stall onset. At every tested pitch rate, the airfoil operating under turbulent inflow conditions stalled at higher angles than under the baseline inflow condition. The angular offset between the baseline inflow condition and the inflow generated by the fine grid ($M = 45$ mm) remains approximately constant to $\Delta\alpha = 3.3 \pm 0.4$ across the full range of pitch rates. This offset is close to the difference measured between the static stall angles of these two inflow conditions. The stall angles measured under the inflow generated by the medium and coarse grids follow the same increasing trend with non-dimensional pitch rate $(\dot{\alpha}c)/(2U_\infty)$, although with larger fluctuations due to higher turbulence intensity in the free-stream. The higher angles of attack at stall also affect the maximum lift coefficients.

The maximum lift coefficient at stall $C_{L,max}$ increases with pitch rate $(\dot{\alpha}c)/(2U_\infty)$ for all configurations (fig. 3b). At low pitch rates, the airfoil operating under turbulent inflow conditions reaches higher maximum lift coefficients than under the baseline inflow condition. As the pitch rate $(\dot{\alpha}c)/(2U_\infty)$ increases, the difference between peak values becomes less

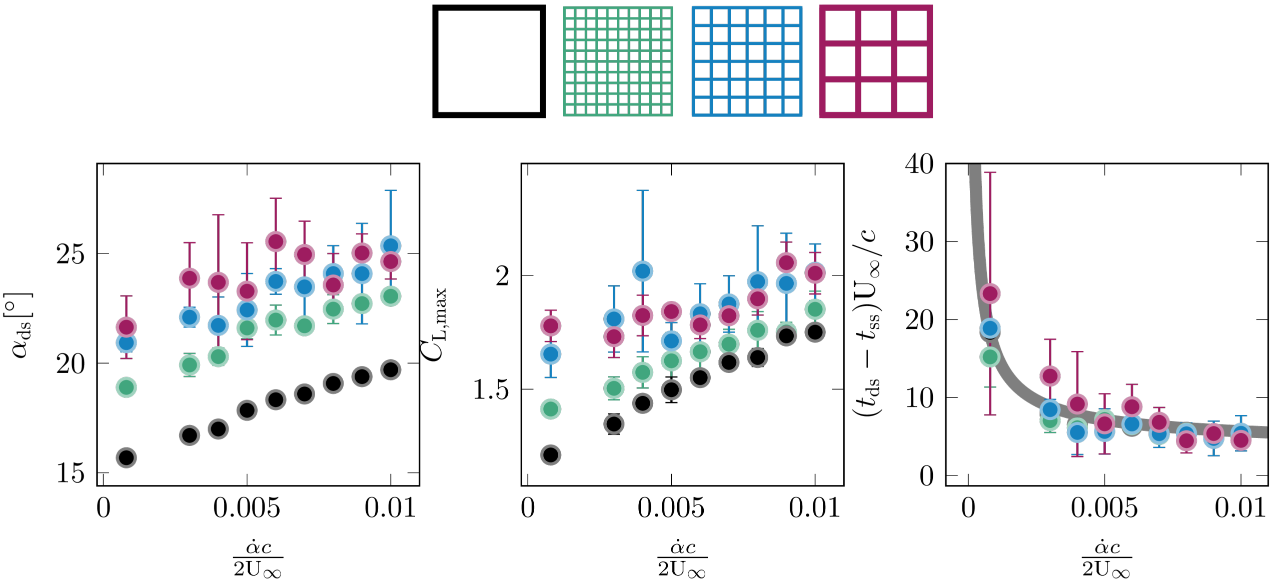

Figure 3. Effect of turbulence on (a) stall onset angle, (b) maximum lift, and (c) stall delay. Results are compared to the no grid condition. The empirical power law stall delay for the baseline low-turbulent flow is shown in panel (c) for comparison. Error bars show the standard deviation of the results over five repetitions.

significant. The peak lift at stall results from the combined contribution of the leading-edge vortex and the angle of attack at which stall occurs. Under turbulent inflow, stall occurs at higher angles of attack across all pitch rates. If the leading-edge vortex strength remained unchanged, these higher stall angles would produce higher peak lift coefficients. The convergence of the maximum lift coefficients despite the higher stall angles indicates that turbulent inflow reduces the effective strength or coherence of the leading-edge vortex. This interpretation is consistent with flow field measurements by Yu *et al.*, whose circulation data show that the peak dimensionless leading-edge vortex circulation decreases under turbulent inflow across a range of reduced frequencies. Damiola *et al.* also reported a less coherent and less detectable dynamic stall vortex under high free-stream turbulence. At low pitch rates ($(\dot{\alpha}c)/(2\mathrm{U}_\infty) = 0.003$), the peak lift remains higher under turbulent inflow because delayed separation allows the airfoil to reach higher angles of attack before stall. At higher pitch rates, vortex-induced lift dominates the peak value, and the reduced vortex coherence limits further lift increase despite the higher stall angle. To assess whether turbulence affects vortex formation timing, we examine the temporal development of dynamic stall.

We quantify the temporal development of dynamic stall using the stall onset delay, defined as the convective time elapsed between the moment the critical stall angle is exceeded and the onset of dynamic stall (fig. 3c). The delays for each inflow condition are measured relative to the corresponding static stall angle determined in fig. 1. The delay values for the baseline and turbulent flow conditions are comparable over the entire range of $(\dot{\alpha}c)/(2\mathrm{U}_\infty)$. The measured delays follow the empirical power-law scaling established for the baseline inflow condition (Rezapour & Mulleners, 2025), given by

$$(t_{\mathrm{ds}} - t_{\mathrm{ss}})\,\frac{\mathrm{U}_\infty}{c} = 0.06\left((\dot{\alpha}c)/(2\mathrm{U}_\infty)\right)^{-0.77} + 3.57. \qquad (1)$$

The constant term represents the characteristic vortex formation time, expressed in convective time units. The agreement between the delay values for all inflow conditions indicates that turbulent inflow shifts the static stall threshold but does not alter the rate-dependent scaling of the stall onset delay or the vortex formation time. This result shows that turbulence modifies the angular stall threshold without affecting the temporal mechanism governing vortex formation and dynamic stall onset. Once the static stall threshold corresponding to each inflow condition is exceeded, the subsequent temporal evolution toward dynamic stall follows the same power-law scaling found for various airfoils and Reynolds numbers (Ayancik & Mulleners, 2022).

4 Conclusion

This work examined how grid-generated free-stream turbulence modifies static and dynamic stall onset at $Re = 60\,000$. Turbulence intensity and integral length scales were varied, and their influence on stall characteristics was investigated. The tested turbulence conditions correspond to integral length scales smaller than the airfoil chord.

Free-stream turbulence shifted both the critical stall angle and the critical reattachment angle to higher angles of attack. The mean lift response in the attached-flow regime remained unchanged, but turbulent inflow increased lift fluctuations due to velocity perturbations in the incoming flow.

Under dynamic pitching, free-stream turbulence delayed stall onset to higher angles of attack across the full range of non-dimensional pitch rates. Turbulent inflow also increased the maximum lift coefficient at low pitch rates, but the difference in peak lift decreased at higher pitch rates. When stall onset delay was measured relative to the quasi-steady stall threshold specific to each inflow condition, the delay followed the same power-law scaling with non-dimensional pitch rate independent of the turbulence level. Free-stream turbulence shifts the stall threshold but preserves the convective timescale governing the onset of dynamic stall. Once the quasi-steady stall threshold is exceeded, the subsequent temporal evolution toward vortex formation and dynamic stall follows the same rate-dependent scaling regardless of turbulence intensity. This robustness further supports that the dynamic stall process is governed by a configuration-dependent threshold and a universal temporal scaling.

The grids used in this study simultaneously increase turbulence intensity and integral length scale with increasing mesh size. The effects of these two parameters on stall onset cannot be separated in the current dataset. All tested integral length scales remain smaller than the airfoil chord ($L/c < 0.4$), a regime in which turbulence intensity governs the aerodynamic response and the integral length scale plays a secondary role (Vita *et al.*, 2020). Wind tunnel experiments on a wind turbine aerofoil with independently varied turbulence intensity and integral length scale show that the strongest aerodynamic effects occur when the integral length scale is comparable to the chord ($L/c \approx 1$), and that a critical turbulence intensity must be exceeded before the length scale modifies the stall behaviour (Vita *et al.*, 2020). Whether the power-law scaling of dynamic stall onset delay is preserved when $L/c \geq 1$, or when turbulence intensity and integral length scale are varied independently, remains an open question. Experiments with multiple grid-to-airfoil distances that decouple these parameters would clarify the respective roles of turbulence intensity and integral length scale on the dynamic stall process.

REFERENCES

Ahmadi-Baloutaki, Mojtaba, Carriveau, Rupp & Ting, David S-K 2015 Performance of a vertical axis wind turbine in grid generated turbulence. *Sustainable Energy Technologies and Assessments* **11**, 178–185.

Ayancik, Fatma & Mulleners, Karen 2022 All you need is time to generalise the Goman–Khrabrov dynamic stall model. *Journal of Fluid Mechanics* **942**, 1–11.

Damiola, Luca, Siddiqui, Muhammad Faheem, Runacres, Mark Charles & De Troyer, Tim 2023 Influence of free-stream turbulence intensity on static and dynamic stall of a NACA 0018 aerofoil. *Journal of Wind Engineering and Industrial Aerodynamics* **232**, 105270.

Dar, Arslan Salim, Waridel, Fabien & Porté-Agel, Fernando 2025 Effect of roof fence shape on flow over a building and its impact on wind turbine performance. *Renewable Energy* **238**, 121859.

Devinant, Ph., Laverne, T. & Hureau, J. 2002 Experimental study of wind-turbine airfoil aerodynamics in high turbulence. *Journal of Wind Engineering and Industrial Aerodynamics* **90** (6), 689–707.

Fransson, Jens H. M. & Shahinfar, Shahab 2020 On the effect of free-stream turbulence on boundary-layer transition. *Journal of Fluid Mechanics* **899**, A23.

Gandhi, Anurag, Merrill, Brandon & Peet, Yulia T. 2017 Effect of Reduced Frequency on Dynamic Stall of a Pitching Airfoil in a Turbulent Wake. In *55th AIAA Aerospace Sciences Meeting*. Grapevine, Texas: American Institute of Aeronautics and Astronautics.

Henne, Sabrina, Parikh, Agastya, Deparday, Julien & Mulleners, Karen 2018 Dynamic stall vortex shedding and associated load fluctuations. In *19th International Symposium of the Applications of Laser and Imaging Techniques to Fluid Mechanics*.

Huang, X., Albers, M., Meysonnat, P.S., Meinke, M. & Schröder, W. 2020 Analysis of the effect of freestream turbulence on dynamic stall of wind turbine blades. *International Journal of Heat and Fluid Flow* **85**, 108668.

Istvan, Mark S. & Yarusevych, Serhiy 2018 Effects of free-stream turbulence intensity on transition in a laminar separation bubble formed over an airfoil. *Experiments in Fluids* **59** (3), 52.

Kay, Nicholas J., Richards, Peter J. & Sharma, Rajnish N. 2020 Influence of Turbulence on Cambered and Symmetrical Airfoils at Low Reynolds Numbers. *AIAA Journal* **58** (5), 1913–1925.

Le Fouest, Sébastien, Deparday, Julien & Mulleners, Karen 2021 The dynamics and timescales of static stall. *Journal of Fluids and Structures* **104**, 103304.

Le Fouest, Sébastien & Mulleners, Karen 2022 The dynamic stall dilemma for vertical-axis wind turbines. *Renewable Energy* **198**, 505–520.

Mishra, Rishabh, Neunaber, Ingrid, Guilmineau, Emmanuel & Braud, Caroline 2022 Wind tunnel study: is turbulent intensity a good candidate to help in bypassing low Reynolds number effects on 2d blade sections? *Journal of Physics: Conference Series* **2265** (2), 022095.

Mohamed, Mohsen S. & Larue, John C. 1990 The decay power law in grid-generated turbulence. *Journal of Fluid Mechanics* **219**, 195–214.

Nedic, Jovan, Fernex, Daniel & Mulleners, Karen 2024 Interaction of freestream turbulence with vortex structures in vertical axis turbines. In *13th International Symposium on Turbulence and Shear Flow Phenomen*. Montreal, Canada: 13th International Symposium on Turbulence and Shear Flow Phenomen.

Porté-Agel, Fernando, Bastankhah, Majid & Shamsoddin, Sina 2020 Wind-Turbine and Wind-Farm Flows: A Review. *Boundary-Layer Meteorology* **174** (1), 1–59.

Revaz, Tristan & Porté-Agel, Fernando 2024 Effect of hills on wind turbine flow and power efficiency: A large-eddy simulation study. *Physics of Fluids* **36** (9), 095180.

Rezapour, Sahar & Mulleners, Karen 2025 Dynamic stall characteristics and modelling of time-varying pitching kinematics. *arXiv preprint arXiv:2508.10647* .

Rezapour, Sahar & Mulleners, Karen 2026 Dynamic stall reattachment revisited. *Journal of Fluid Mechanics* **1029**, A52.

Shamsoddin, Sina & Porté-Agel, Fernando 2018 Wind turbine wakes over hills. *Journal of Fluid Mechanics* **855**, 671–702.

Thompson, C., Biler, H., Symon, S. & Ganapathisubramani, B. 2023 Effects of integral length scale variations on the stall characteristics of a wing at high free-stream turbulence conditions. *Journal of Fluid Mechanics* **974**, A9.

Toppings, Connor & Yarusevych, Serhiy 2025 Low-Reynolds-number aerofoil boundary layer transition in large-scale free stream turbulence. *Journal of Fluid Mechanics* **1021**, A46.

Vahidi, Dara & Porté-Agel, Fernando 2024 Potential of wake scaling techniques for vertical-axis wind turbine wake prediction. *Energies* **17** (17), 4527.

Vita, Giulio, Hemida, Hassan, Andrianne, Thomas & Baniotopoulos, Charalampos 2020 The effect of the integral length scale of turbulence on a wind turbine aerofoil. *Journal of Wind Engineering and Industrial Aerodynamics* **204**, 104235.

Yu, J. M., Leu, T. S. & Miau, J. J. 2017 Investigation of reduced frequency and freestream turbulence effects on dynamic stall of a pitching airfoil. *Journal of Visualization* **20** (1), 31–44.